nature photonics

Article

https://doi.org/10.1038/s41566-024-01592-y

Observation of loss-enhanced magneto-optical effect

Received: 1 January 2024

Accepted: 4 November 2024

Published online: 19 December 2024

Check for updates

Ya-Ping Ruan[1,8], Jiang-Shan Tang[1,8], Zhipeng Li[2,8], Haodong Wu[1], Wenpeng Zhou[1], Longqi Xiao[1], Jianfeng Chen[2], Shi-Jun Ge[1], Wei Hu[1], Han Zhang[3], Cheng-Wei Qiu[2] ✉, Wuming Liu[4] ✉, Hui Jing[5,6] ✉, Yan-Qing Lu[1] ✉ & Keyu Xia[1,7] ✉

Magneto-optical (MO) effects have a pivotal role in modern photonic devices for light manipulation and sensing, but the study of these effects has so far been limited to the MO Faraday and Kerr effects. Conventional MO systems encounter considerable intrinsic losses, markedly hampering their ability to amplify the MO effects. Here we introduce a loss-enhanced MO effect to sublinearly amplify the frequency response of a non-Hermitian optical cavity under different background magnetic fields. This exceptional MO effect relies on an architecture of MO material embedded in a Fabry–Pérot cavity, accompanied by a polarization-dependent optical absorption, that is, linear dichroism, to construct a reconfigurable exceptional point. The experimental results show that two eigenmodes of the Fabry–Pérot cavity exhibit sublinear frequency splitting. By electrically reconfiguring the absorber, the eigenfrequency shift can be adaptively enhanced under different background magnetic fields. Using this effect, we demonstrate the detection of subtle magnetic field variations in a strong background, with the system's response magnified by a factor exceeding 10 and sensitivity increased threefold compared with its conventional Hermitian counterpart. Our study leverages exceptional physics to study the MO effect and develops a new class of reconfigurable MO devices equipped with enhanced sensitivity for potential integration with photonic systems.

Magneto-optical (MO) effects are pivotal in electromagnetism and quantum mechanics[1], finding widespread applications in photonics for sensing, non-reciprocal devices, spintronics, magnetism of two-dimensional materials, quantum computation and the identification of fundamental physical effects[2–7]. So far, they have been mostly limited to the conventional MO Faraday and Kerr effects. Both originate from the magnetically modified dielectric tensor and are manifested by the polarization rotation and ellipticity, as a linear response, of linearly polarized light transmitting through or reflected off an MO medium under a static magnetic field[8]. Conventional MO devices rely on strong MO materials and physically bulky devices[9], hindering their seamless integration into photonic systems. Although two-dimensional materials show strong MO Faraday or Kerr effects[5,10], their practical use is impeded by the necessity for extremely low temperature and ultrahigh magnetic fields. Furthermore, although nanophotonic structures show enhanced MO effects at room temperature[11,12], the demands of intricate

[1]College of Engineering and Applied Sciences, National Laboratory of Solid State Microstructures, Nanjing University, Nanjing, China. [2]Department of Electrical and Computer Engineering, National University of Singapore, Singapore, Singapore. [3]School of Physics, Nanjing University, Nanjing, China. [4]Beijing National Laboratory for Condensed Matter Physics, Institute of Physics, Chinese Academy of Sciences, Beijing, China. [5]Key Laboratory of Low-Dimensional Quantum Structures and Quantum Control of Ministry of Education, Department of Physics and Synergetic Innovation Center for Quantum Effects and Applications, Hunan Normal University, Changsha, China. [6]Institute for Quantum Science and Technology, College of Science, National University of Defense Technology, Changsha, China. [7]Hefei National Laboratory, Hefei, China. [8]These authors contributed equally: Ya-Ping Ruan, Jiang-Shan Tang, Zhipeng Li. ✉e-mail: chengwei.qiu@nus.edu.sg; wmliu@iphy.ac.cn; jinghui@hunnu.edu.cn; yqlu@nju.edu.cn; keyu.xia@nju.edu.cn

https://doi.org/10.1038/s41566-024-01592-y

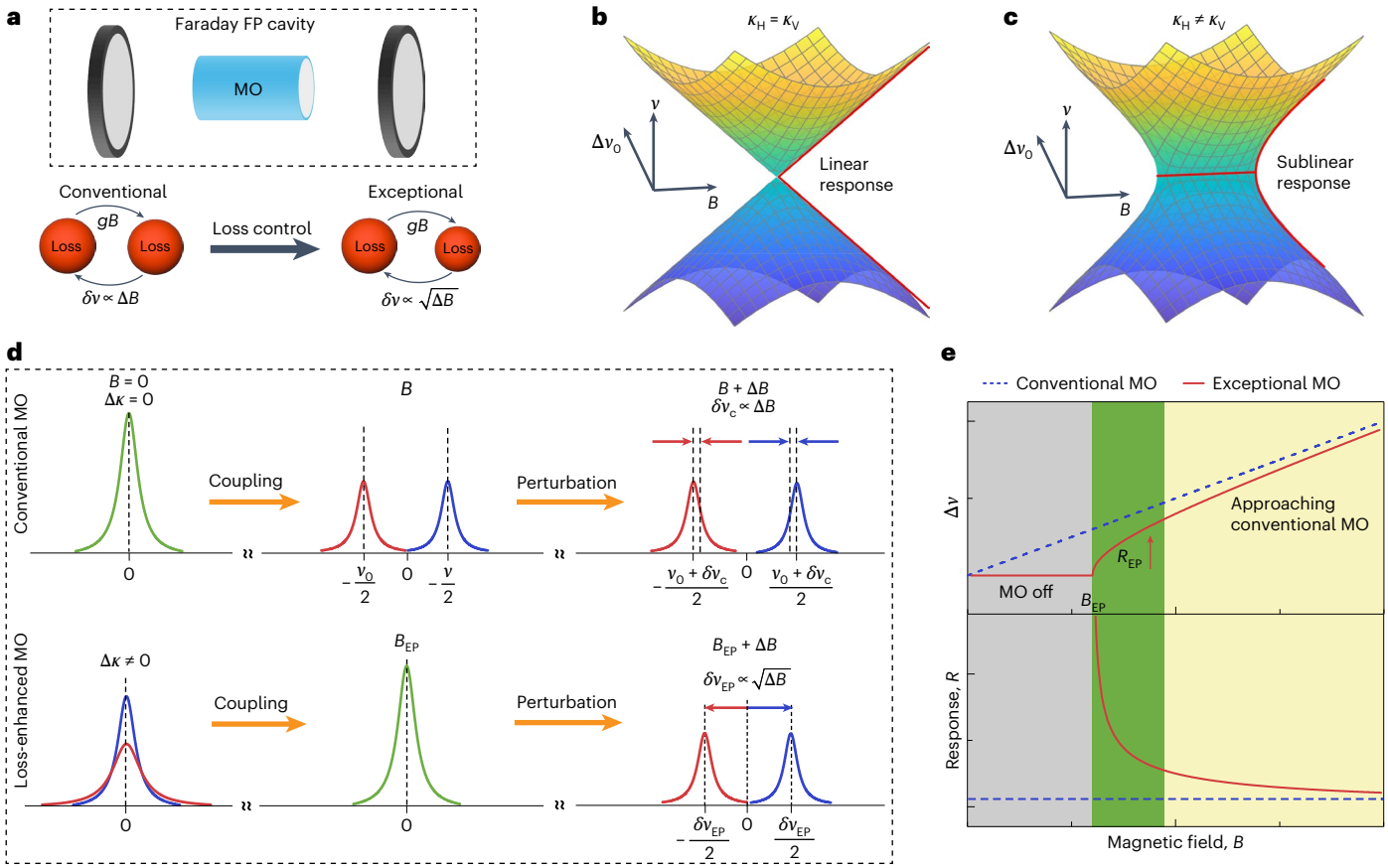

Fig. 1 | Loss-enhanced MO effect. a, Conceptual illustrations of loss-controlled MO effect. A conventional Hermitian system consists of an MO Faraday material in an FP cavity, where the losses of two orthogonal modes remain equal. The resonant frequencies of the two modes show a linear function with magnetic field perturbation. An additional loss is inserted into the cavity to break the parity symmetry and create a reconfigurable EP, resulting in an enhanced MO effect due to sublinear frequency split induced by the loss. **b**,**c**, The real part, Re[ν], of the two eigenfrequency surfaces plotted in ($\Delta\nu_0$, B) parameter space of the conventional (**b**) and loss-enhanced MO effects (**c**). **d**,**e**, An illustration of spectrum features (**d**) and a comparison of frequency splits and response (**e**) of the conventional and loss-enhanced MO effects.

precise nanostructuring involve substantial complexity. A more serious issue in both systems is the intrinsic loss that constrains the MO effects and the quality of the system response[13], posing a fundamental challenge. Efficiently enhancing the MO effects while maintaining miniaturization and reconfigurability remains a highly demanded but challenging task. The MO effects in a non-Hermitian system have been elusive thus far.

Non-Hermitian physics have been widely studied in various bosonic and even quantum systems by sophistically engineering the mode coupling[14–23]. By contrast, the MO effects, modifying the off-diagonal elements of the dielectric tensor, allow one to electrically tune the coupling of two optical cavity modes without interference with the mode resonance frequency, offering an important advantage in flexibility and tunability. Moreover, they also spontaneously break the time-reversal symmetry (TRS), which gives rise to a great number of remarkable fundamental physical phenomena. Thus, the MO system can be an ideal platform for the study of non-Hermitian physics[24]. Recently, magnetic-related non-Hermitian systems, such as magnonic waveguides and cavities and quantum spins, have been proposed to unveil exotic physics[21,25–29]. Among these phenomena, special singularity points termed exceptional points (EPs) have garnered considerable interest due to the simultaneous coalescence of both eigenvalues and eigenvectors[30].

One main workhorse of studying non-Hermitian physics is the potential improvement of the sensor responsivity[31–34] and the stability[35] near EPs. The concept is theoretically proposed by Wiersig[36], stimulating intensive attention. Through exploring EPs in completely passive systems, the detrimental loss has been transformed into an advantageous factor for various phenomena[37–42], particularly in sensing[43]. However, it remains unclear whether an EP can amplify a sensor's sensitivity[44–48], mainly because of the equal enhancement of gain-induced noise. Nonetheless, constraint to the noise enhancement in a passive non-Hermitian system becomes a major subject of further study of EP sensors[44]. EPs in MO systems beyond (quasi-)particle contexts[21,25–29,35] are also yet to be explored.

Here, we introduce a loss-enhanced MO effect. Differing from the linear polarization rotation of light in the MO Faraday and Kerr effects, its response near EPs is identified as a sublinear eigenfrequency splitting of an optical cavity under various background magnetic fields. To demonstrate this exceptional MO effect, we construct a non-Hermitian system by inserting an MO material in a Fabry–Pérot (FP) cavity, thus breaking the TRS. Note that the magnetically modified dielectric tensor causes the non-reciprocal coupling between two orthogonal cavity modes. We further break the parity symmetry by introducing additional unbalanced polarization-dependent losses—otherwise challenging to overcome—to the two orthogonal modes of the FP cavity (Fig. 1). An EP emerges when the degree of broken parity symmetry matches that of broken TRS, leading to the degeneracy of two eigenfrequencies. We then demonstrate that a subtle magnetic field variation, superimposed on a relatively strong bias, leads to a sublinear eigenfrequency splitting that is enhanced by a factor exceeding 10 compared with the conventional Hermitian MO configuration[49] (Fig. 1).

https://doi.org/10.1038/s41566-024-01592-y

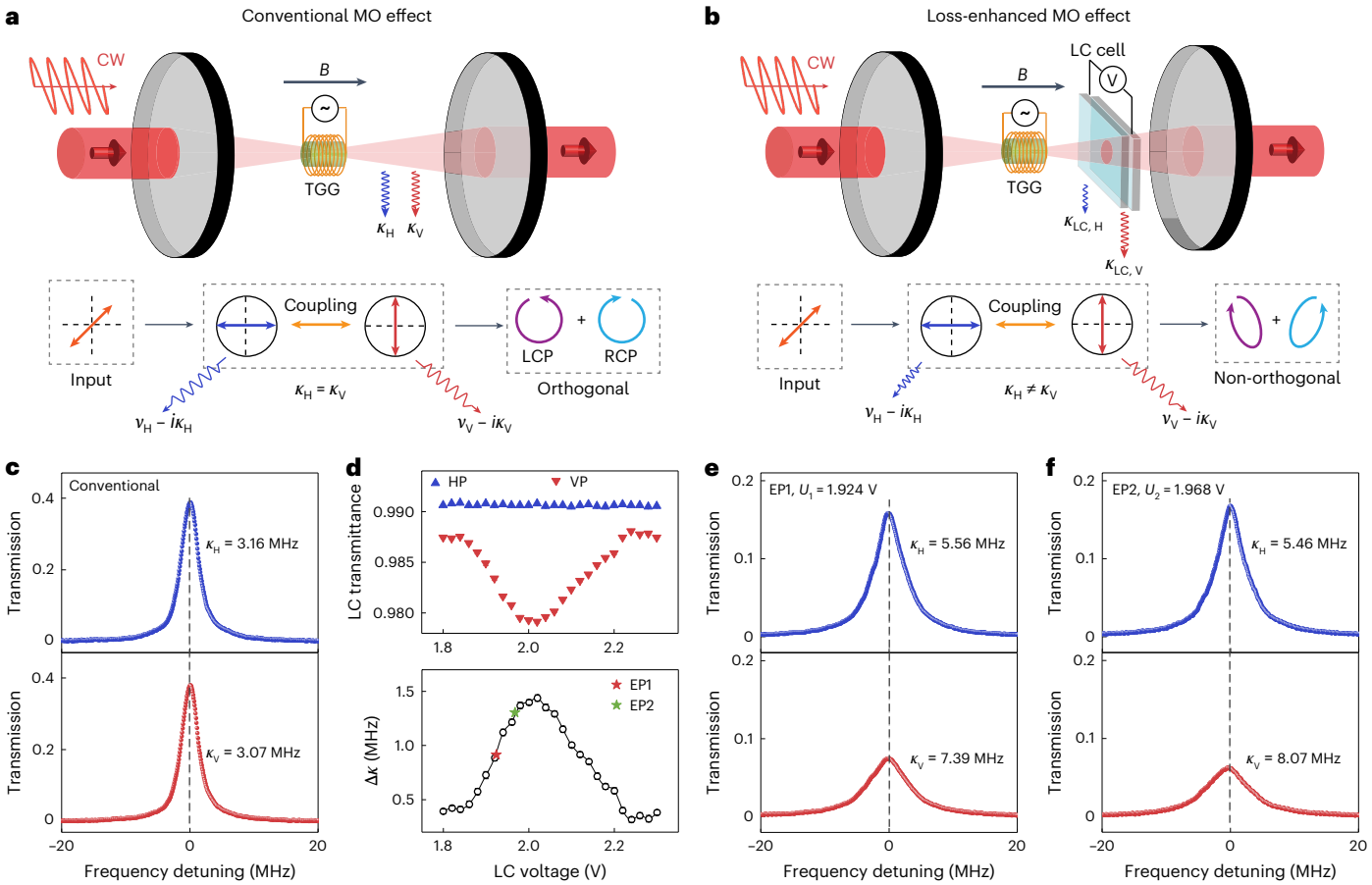

Fig. 2 | Experimental setup and characterization. a,b, Schematics of experimental setups for the conventional Hermitian MO effect (**a**) and the loss-enhanced MO effect (**b**) under a linearly polarized continuous-wave (CW) input. **c**, Transmission spectra of the HP (blue curve) and VP (red curve) modes in the conventional setup. The two modes show approximately equal decay rates. **d**, Single-pass transmittance of the LC cell (top) and calculated loss difference $\Delta\kappa$ (bottom) versus the applied voltage U in free space. Two EPs (EP1 shown as red stars and EP2 as green stars) emerge under different magnetic fields. **e**,**f**, Transmission spectra of the HP and VP modes at EP1 with $\Delta\kappa = 0.92$ MHz (**e**) and EP2 with $\Delta\kappa = 1.31$ MHz (**f**).

In contrast to the gain–loss counterpart, a threefold improvement in sensitivity is achieved. As the linear dichroism of the additional optical absorber can be electrically controlled, the achieved amplification of the MO effect can be reconfigured to adapt to different background magnetic fields.

Theory

Figure 1 shows the basic concepts of the conventional Hermitian and loss-enhanced MO effects, along with their responses to a magnetic perturbation ΔB. Both setups consist of an FP optical cavity and an embedded MO material (Fig. 1a). The cavity supports the horizontally and vertically polarized (denoted as HP and VP) modes with frequencies ν_H and ν_V, and decay rates κ_H and κ_V, respectively. Due to the magnetization of a magnet[50], the MO material induces a coupling between the HP and VP modes with a strength gB, which is proportional to the amplitude of the applied d.c. magnetic field **B**. The coefficient g is determined by the Verdet constant of the MO material and the geometry (Methods). We neglect the small magnetically induced absorption and assume that g is a real number because its imaginary part is at least two orders of magnitude smaller (Supplementary Section 2). The MO system spontaneously breaks the TRS, described by a non-Hermitian Hamiltonian (Methods and Extended Data Fig. 1)

$$H = h\begin{bmatrix} \nu_H - i\kappa_H & igB \\ -igB & \nu_V - i\kappa_V \end{bmatrix}, \quad (1)$$

where h is the Planck's constant. This Hamiltonian is derived in a quantum formalism. It provides a transparent picture necessary for understanding the mode coupling of a cavity and can reveal rich physics beyond the classical picture of circular birefringence. The eigenfrequencies can be calculated as

$$\nu_\pm = \nu_0 - i\kappa \pm \sqrt{g^2B^2 + (\Delta\nu_0 + i\Delta\kappa)^2}, \quad (2)$$

where $\nu_0 = (\nu_H + \nu_V)/2$, $\Delta\nu_0 = (\nu_H - \nu_V)/2$, $\kappa = (\kappa_V + \kappa_H)/2$ and $\Delta\kappa = (\kappa_V - \kappa_H)/2$. $\Delta\nu_0$ and $\Delta\kappa$ are respectively the frequency difference and loss difference between the HP and VP modes in the absence of the magnetic field, meaning $B = 0$. The frequency response of the system is measured as the eigenfrequency splitting, $\Delta\nu = \Re[\nu_+] - \Re[\nu_-]$. Here, $\Re[\cdot]$ means the real part of a complex number. The capability of sensing a small fluctuation ΔB relies on the dynamic response of a sensor operating at a bias B. Here, the dynamic response is evaluated as the response slope $R = \partial\Delta\nu/\partial B$.

We start from explaining the conventional Hermitian MO effect with $\kappa_H = \kappa_V$ and $\Delta\nu_0 = 0$ as schematically illustrated in Fig. 1a. The system's response $\nu_\pm$ is always a linear function of B (see the corresponding eigenfrequency surface in Fig. 1b) In the absence of a background magnetic field, the spectra of the two modes in the conventional system overlap due to their equal resonant frequencies and loss rates (Fig. 1d). Upon coupling by a background magnetic field B, the spectra of the conventional system split. A small magnetic perturbation further separates the two spectra, resulting in linearly shifted resonant frequencies.

https://doi.org/10.1038/s41566-024-01592-y

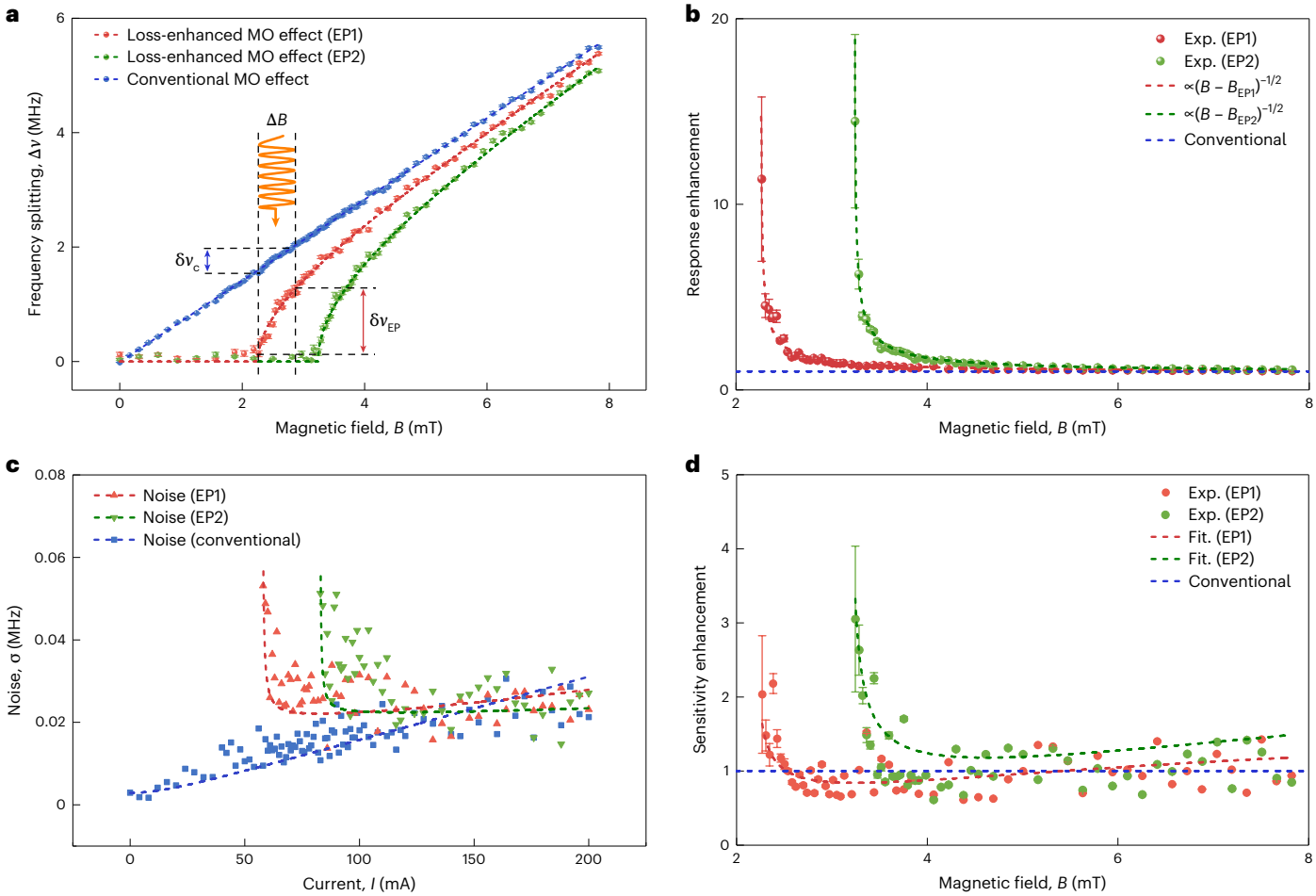

Fig. 3 | Observation of the conventional Hermitian MO effect and the loss-enhanced MO effect. a, The eigenfrequency split of the two MO effects versus the magnetic fields. The filled dots and dashed curves represent the experimental data (Exp.) and the fitting results (Fit.), respectively. **b**, The response enhancement of the loss-enhanced MO effect in comparison with the conventional Hermitian MO effect. **c**, Noise measured as the one-standard-deviation (1σ) uncertainty in two systems as a function of the applied current I, obtained from ten independent repeated measurements. **d**, Sensitivity enhancement of the loss-enhanced MO effect. The data points and error bars are presented as the mean values and the 1σ uncertainty, respectively, obtained from ten independent repeated experiments.

The eigenfrequency splitting is $\Delta\nu_c = 2gB$, yielding a constant dynamic response $R_c = \partial\Delta\nu_c/\partial B = 2g$ to the perturbation (Fig. 1e). Considering a weak magnetic perturbation ΔB, the MO effect cannot be effectively amplified in this conventional configuration.

Now we introduce the loss-enhanced MO effect to address the aforementioned challenges. We further break the parity symmetry by adding the differential loss between the HP and VP modes with a liquid crystal (LC) cell such that $\Delta\kappa \neq 0$. By stark contrast, the response of loss-enhanced MO effect is essentially different from the conventional Hermitian counterpart (Fig. 1c). We consider the case of $\Delta\nu_0 = 0$. The spectrum features of the HP and VP modes under the zero magnetic field illustrate the unbalanced losses (Fig. 1d). When the degree of broken parity symmetry equals that of broken TRS, that is, $B_{EP} = |\Delta\kappa|/g$, an EP emerges where both eigenvalues and eigenvectors simultaneously coalesce. The spectra of the two modes in Fig. 1d show a gradually overlapped feature, indicating the degenerated real parts and imaginary parts of eigenfrequencies at the EP. When $B > B_{EP}$, the system is in the so-called passive parity–time (PT) symmetric phase without involving gain[51]. The eigenfrequencies $\nu_\pm$ transform into a nonlinear function of B (equation (2)). The resultant eigenfrequency splitting is $\Delta\nu_{EP} = 2\sqrt{g^2B^2 - \Delta\kappa^2}$. The dynamic response at B is given by $R_{EP} = \frac{\partial\Delta\nu_{EP}}{\partial B}|_{B>B_{EP}} = 2g^2B/\sqrt{g^2B^2 - \Delta\kappa^2}$ (Fig. 1e). For a small perturbation ΔB around B_{EP}, the dynamic response is amplified by a factor of approximate $\sqrt{B_{EP}/2\Delta B}$ ($B_{EP} = |\Delta\kappa|/g$) in comparison with the conventional Hermitian case with preserved parity symmetry. Clearly, a larger $\Delta\kappa$, corresponding to a stronger B_{EP}, leads to a higher response enhancement near the EP[52,53]. This enhancement highlights how the loss-enhanced MO effect enables highly sensitive measurements of a weak magnetic fields against a strong background. After the parity symmetry is sufficiently broken $B < B_{EP}$, the real parts of eigenfrequencies remain unsplit, showing a suppressed frequency response under a background magnetic field. It is worth noting that the degree of broken parity symmetry can be electrically controlled, thereby allowing for reconfiguration of these exceptional performances adaptive to different background magnetic fields.

The sensor sensitivity is evaluated as the ratio of measurement uncertainty, namely, noise, and the response[54], that is, $S_c = \sigma_c/R_c$ and $S_{EP} = \sigma_{EP}/R_{EP}$, where σ_c and σ_{EP} respectively denote noise in the conventional Hermitian and loss-enhanced MO effects. The enhancement factor of sensitivity is then given by $G_S = S_c/S_{EP} = G_R \times \sigma_c/\sigma_{EP}$.

Experiments

The experimental setups for the conventional Hermitian and loss-enhanced MO effects are schematically shown in Fig. 2a,b (see Supplementary Section 1 and Supplementary Fig. 1 for the setup). In both systems, the FP cavity is composed of two highly reflective mirrors

https://doi.org/10.1038/s41566-024-01592-y

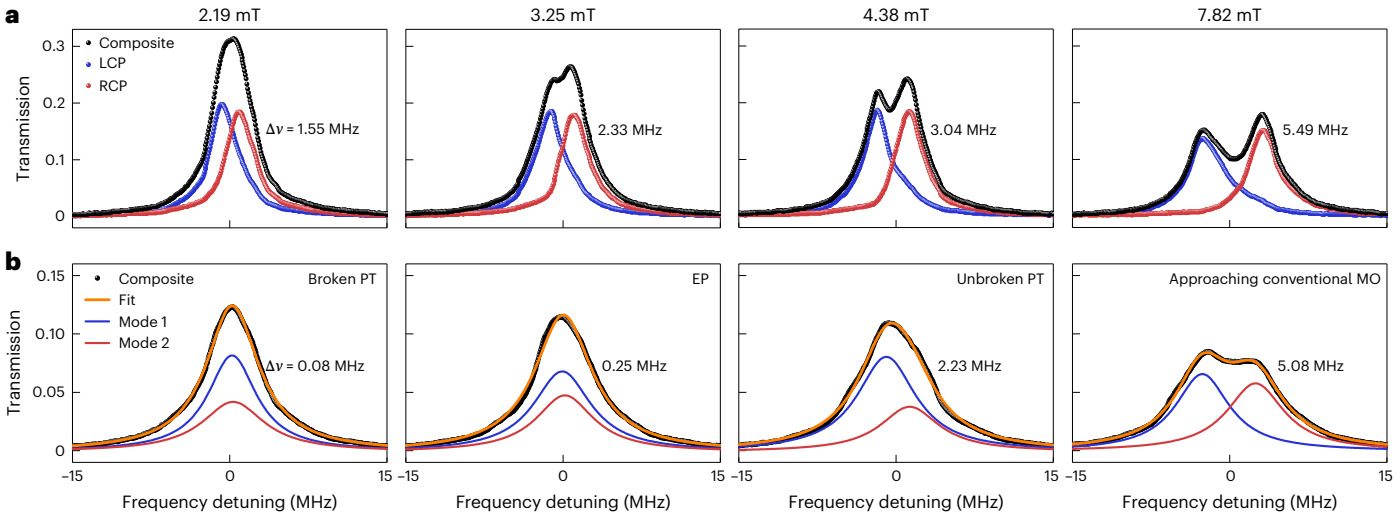

Fig. 4 | Transmission spectra under different magnetic fields. a, The conventional Hermitian MO effect. The LCP (blue balls) and RCP (red balls) transmission spectra are measured separately by two photodetectors and fitted with Lorentzian profiles. The frequency split is linear to the magnetic fields. **b**, The loss-enhanced MO effect. The transmission spectra of the composite fields is measured (black dots) and fitted with two Lorentzian profiles (solid orange curves). EP2 emerges at a magnetic field of 3.24 mT. The frequency split is nonlinear to the magnetic fields. The small split at EP is caused by experimental imperfection.

with reflectivity of 99%. Each mirror induces an external loss with rate κ_e. A Faraday MO medium, made from (111)-cut cylindrical terbium gallium garnet (TGG) crystal, is inserted into the cavity to induce the coupling between the HP and VP modes via a background magnetic field and the MO effect. The magnetic field is created by electrical current I in the coil surrounding the TGG crystal. In the absence of magnetic field, the resonant frequencies of HP and VP modes are equal such that $\Delta\nu_0 = 0$. The coupling strength is an imaginary value given by igB where the coefficient g is proportional to the Verdet constant, measured to be 78.82 rad T^{-1} m^{-1} (Methods and Extended Data Fig. 2). The HP and VP modes exhibit the same dissipation rate in the Hermitian system for the conventional MO effect (Fig. 2a). By contrast, the loss-enhanced MO effect relies on a very large loss difference, which is the key requirement for exhibiting the EP but challenging. To tackle this challenge, an LC is inserted in the FP cavity to induce a tunable differential loss, that is, $\Delta\kappa \neq 0$, between the HP and VP modes even when $B = 0$ (Fig. 2b).

To study the loss-enhanced MO effect, we project a continuous-wave laser with frequency ν, linearly polarized at 45° with respect to the horizontal plane and centred at 795 nm, to the MO cavity and observe the total transmission spectra. In this configuration, both the HP and VP modes are driven. The output power spectral lineshape of non-Hermitian systems may exhibit either Lorentzian or super-Lorentzian profiles near EP ($g\Delta B \ll \kappa$)[55]. When a single cavity mode is excited, the total output power spectrum exhibits a squared Lorentzian lineshape[56]. However, in our scenario where two cavity modes are simultaneously excited, the transmission spectrum approximates the superposition of two Lorentzian lineshapes near EP (Supplementary Section 3 and Supplementary Fig. 3)

$$T \approx \left(1 - \frac{2g\Delta B\Delta\kappa}{\kappa^2}\right)\left[\frac{2\kappa_e^2}{\Delta_+^2 + \kappa_+^2} + \frac{2\kappa_e^2}{\Delta_-^2 + \kappa_-^2}\right], \qquad (3)$$

where $\Delta_\pm = \nu - \mathcal{R}[\nu_\pm]$ and $\kappa_\pm = -\mathcal{I}[\nu_\pm]$. $\mathcal{I}[\cdot]$ denotes the imaginary part of a complex number. Ideally, $\kappa_+ = \kappa_- = \kappa$. This approximation is always met in our experiment ($B \leq 7.82$ mT). The frequency response can be retrieved by fitting the total transmission spectrum with the sum of two Lorentzian lineshapes. By contrast, the eigenspectra of the conventional MO sensor are measured by separating the left circular polarization (LCP) and right circular polarization (RCP) components, each of which can be individually fitted with a Lorentzian lineshape.

We first observe the conventional Hermitian MO effect with the preserved parity symmetry. κ_H and κ_V are designed to be equal for the HP and VP cavity modes at $B = 0$, but measured to be 3.16 MHz and 3.07 MHz (Fig. 2c), respectively, due to experimental imperfections. The loss difference $\Delta\kappa = 0.045$ MHz is negligible. In the presence of an external magnetic field B (Fig. 3a), the two eigenmodes become LCP and RCP with eigenfrequencies $\nu_\pm = \nu_0 \pm gB$. The conventional MO effect shows a linear frequency response as a function of B, also illustrated by the transmission spectra in Fig. 4a. This result indicates a weak MO effect under an external magnetic field $B < 8$ mT. In addition, conventional MO configuration lacks the reconfigurability to amplify the MO effect.

We now observe the loss-enhanced MO effect by further breaking the parity symmetry. We introduce considerably distinct losses to the HP and VP modes by using an LC cell with a molecular alignment tuned with an electrical voltage U (Fig. 2b and Supplementary Section 4). In this case, the two eigenmodes become elliptically polarized and non-orthogonal. Figure 2d shows differential absorption of the LC for the HP and VP light, that is, linear dichroism, for a single pass. The loss difference $\Delta\kappa$ is comparable to the decay rates of the cavity modes. In our two trials, $\Delta\kappa$ is set to be 0.92 MHz and 1.31 MHz (Fig. 2e,f), corresponding to EP1 and EP2 shown in Fig. 2d.

The loss-enhanced MO effect is shown in Fig. 3. When the degree of broken TRS is smaller than that of broken parity symmetry, the frequency split is completely switched off even though the external magnetic field ($0 < B < B_{EP}$) is present. At EP1 ($B_{EP} = 2.26$ mT, $U = 1.924$ V), the loss-enhanced MO effect is ultrasensitive to subtle magnetic field variations on the base of a strong background, indicated by the square-root response shown by the red dots and corresponding curve in Fig. 3a. Compared with the conventional MO effect, the dynamic response is enhanced by a factor of 11 (Fig. 3b). For $\Delta\kappa = 1.31$ MHz, the EP shifts to $B_{EP} = 3.24$ mT (EP2) (Fig. 3a). The response enhancement increases to a factor of 14 around EP2, in agreement with the theory[52,53]. This response enhancement was considered as the sensitivity improvement of a gain–loss non-Hermitian sensor in previous works[32,33].

The system noise is characterized in Fig. 3c. There are two uncorrelated noise contributions: the I-related noise and the background noise. In our experiment, the overall noise is well fitted by $\sigma_c = \sqrt{\sigma_{0,c}^2 + (\gamma_c I)^2}$ for the conventional Hermitian MO effect and

$\sigma_{EP} = \sqrt{\sigma_{0,EP}^2 + (G_R \gamma_{EP} I)^2}$ for the loss-enhanced MO effect. The fitting parameters are $\gamma_c = 1.547 \times 10^{-4}$ MHz mA^{-1}, $\sigma_{0,c} = 0.0029$MHz, $\gamma_{EP1} = 9.67 \times 10^{-5}$ MHz mA^{-1}, $\sigma_{0,EP1} = 0.019$ MHz and $\gamma_{EP2} = 4.65 \times 10^{-5}$ MHz mA^{-1}, $\sigma_{0,EP2} = 0.021$ MHz for the conventional, EP1 and EP2 sensors, respectively. Enhancement of the response suppresses only the background noise but not the signal-related noise, which is interpreted as the effect of the Petermann factor[44].

The sensitivity enhancement is then evaluated on the basis of the noise and the dynamic response as $G_S = G_R \frac{\sigma_c}{\sigma_{EP}}$. This simple model is in good agreement with experimental results (Fig. 3d). Note that the dynamic response R_c of the Hermitian system is constant across various magnetic fields. Therefore, it is reasonable to compare the performance of two systems around EP. In our experiments, the EP1 sensor obtains twofold enhancement in sensitivity (Fig. 3d). Our experimental results clearly confirm that the sensitivity at a lossy EP can be enhanced, in sharp contrast to the conclusion in refs. 44–46 that the EP sensors cannot perform exceptional sensitivity. In real measurement, the signal is fed into the system externally and the I-related noise is avoided. The sensitivity of the conventional MO effect at the diabolic point is then given by $\sigma_{0,c}/R_c$. Considering this practical case, we evaluate the sensitivity improvement as $G'_S = G_R \frac{\sigma_{0,c}}{\sigma_{0,EP}}$ and obtain $G'_S = 1.7$ for the EP1 and $G'_S = 2.0$ for the EP2. Our non-Hermitian sensor still shows enhancement in sensitivity because its improved response suppresses the inevitable background noise. In principle, the measurement uncertainty is limited by the spectral fitting uncertainty, which is determined by the background noise and given by κ/M with $M \approx 200$. Thus, the attainable sensitivity is $\kappa_{tot}\sqrt{g^2B^2 - \Delta\kappa^2/2Mg^2B}$ within a fixed measurement time, where κ_{tot} is the total loss of the cavity. Near EP, the sensitivity is approximated as $\frac{\kappa_{tot}}{gM}\sqrt{\frac{\Delta B}{2B_{EP}}}$. The sensitivity can be improved if the Ce-doped yttrium iron garnets (Ce:YIG) with $C_v \approx -10^5$ rad T m^{-1} (ref. 9) at 1,550 nm and a cavity with a higher quality factor are applied (Supplementary Section 5).

The loss-enhanced MO effect can be reconfigured to adapt to different background magnetic fields by suppressing the frequency split in the broken PT symmetric phase and amplifying the response to a small fluctuation in the passive PT symmetric phase. This unique property is confirmed by the output spectra shown in Fig. 4. In the conventional MO system, the frequency splitting is a linear function of the magnetic field B (Fig. 4a). Taking a new background magnetic field $B = 3.24$ mT, for example, of the reconfigurable loss-enhanced MO effect (Fig. 4b), we tune the voltage U of the LC to be 1.968 V to reach EP2. The exceptional performances, including a 14-fold enhanced frequency shift at EP2 and the suppressed frequency split before EP2, are preserved as shown in Fig. 3. The suppressed and enhanced frequency splits are also confirmed by the transmission spectra at magnetic fields of 2.19 mT and 4.38 mT in Fig. 4b, respectively. Note that, if the TRS is sufficiently broken, the response of the loss-enhanced MO effect approaches that of the conventional counterpart, as shown by an example at 7.82 mT in Fig. 4.

Conclusions and outlook

We have demonstrated a loss-controlled MO effect with an enhanced dynamic frequency response and electrical reconfigurability to varying background magnetic fields. An additional loss counterintuitively enhances the sensitivity by threefold near EP of a non-Hermitian system. Conclusive evidence has been clearly observed to confirm the advantage of an EP sensor in measurements, a field stimulating vast debates since the pioneering theoretical prediction[36]. This work opens the door to using the interplay between the exceptional MO effect and non-Hermitian physics for making sensors with high sensitivity.

By tuning the EP to screen the unwanted strong background, the sensor can sensitively detect minute fluctuations without requiring magnetic shielding. This scheme is particularly advantageous when magnetic shielding is either inaccessible or costly, such as in mineral exploration or magnetic resonance imaging. The loss-enhanced sensor can also potentially be integrated into an LC microcavity embedded with an iron garnet film such as Ce:YIG[57]. Due to the ultrahigh Verdet constant of Ce:YIG[9], the sensitivity can potentially be improved by three orders of magnitude.

Online content

Any methods, additional references, Nature Portfolio reporting summaries, source data, extended data, supplementary information, acknowledgements, peer review information; details of author contributions and competing interests; and statements of data and code availability are available at https://doi.org/10.1038/s41566-024-01592-y.

References

1. Kimel, A. et al. The 2022 magneto-optics roadmap. *J. Phys. D* **55**, 463003 (2022).
2. Luo, J. et al. Large effective magnetic fields from chiral phonons in rare-earth halides. *Science* **382**, 698–702 (2023).
3. Yavorsky, M. A. et al. Topological Faraday effect for optical vortices in magnetic films. *Phys. Rev. Lett.* **130**, 166901 (2023).
4. Lyalin, I., Alikhah, S., Berritta, M., Oppeneer, P. M. & Kawakami, R. K. Magneto-optical detection of the orbital Hall effect in chromium. *Phys. Rev. Lett.* **131**, 156702 (2023).
5. Dirnberger, F. et al. Magneto-optics in a van der Waals magnet tuned by self-hybridized polaritons. *Nature* **620**, 533–537 (2023).
6. Burch, K. S., Mandrus, D. & Park, J.-G. Magnetism in two-dimensional van der Waals materials. *Nature* **563**, 47–52 (2018).
7. Choi, Y.-G. et al. Observation of the orbital hall effect in a light metal Ti. *Nature* **619**, 52–56 (2023).
8. Zvezdin, A. K. & Kotov, V. A. *Modern Magnetooptics and Magnetooptical Materials* (Taylor & Francis, 1997)
9. Yan, W. et al. Waveguide-integrated high-performance magneto-optical isolators and circulators on silicon nitride platforms. *Optica* **7**, 1555–1562 (2020).
10. Crassee, I. et al. Giant Faraday rotation in single- and multilayer graphene. *Nat. Phys.* **7**, 48–51 (2011).
11. Chin, J. Y. et al. Nonreciprocal plasmonics enables giant enhancement of thin-film Faraday rotation. *Nat. Commun.* **4**, 1599 (2013).
12. Ignatyeva, D. O. et al. All-dielectric magnetic metasurface for advanced light control in dual polarizations combined with high-Q resonances. *Nat. Commun.* **11**, 5487 (2020).
13. Rizal, C., Shimizu, H. & Mejía-Salazar, J. R. Magneto-optics effects: new trends and future prospects for technological developments. *Magnetochemistry* **8**, 94 (2022).
14. Rüter, C. E. et al. Observation of parity–time symmetry in optics. *Nat. Phys.* **6**, 192–195 (2010).
15. Peng, B. et al. Parity–time-symmetric whispering-gallery microcavities. *Nat. Phys.* **10**, 394–398 (2014).
16. Chang, L. et al. Parity–time symmetry and variable optical isolation in active-passive-coupled microresonators. *Nat. Photon.* **8**, 524–529 (2014).
17. Xu, H., Mason, D., Jiang, L. & Harris, J. G. E. Topological energy transfer in an optomechanical system with exceptional points. *Nature* **537**, 80–83 (2016).
18. Chen, H.-Z. et al. Revealing the missing dimension at an exceptional point. *Nat. Phys.* **16**, 571–578 (2020).
19. Peng, P. et al. Anti-parity–time symmetry with flying atoms. *Nat. Phys.* **12**, 1139–1145 (2016).
20. Li, Y. et al. Anti-parity–time symmetry in diffusive systems. *Science* **364**, 170–173 (2019).
21. Wu, Y. et al. Observation of parity–time symmetry breaking in a single-spin system. *Science* **364**, 878–880 (2019).
22. Xiao, L. et al. Non-Hermitian bulk-boundary correspondence in quantum dynamics. *Nat. Phys.* **16**, 761–766 (2020).

23. Wang, Y.-T. et al. Experimental investigation of state distinguishability in parity–time symmetric quantum dynamics. *Phys. Rev. Lett.* **124**, 230402 (2020).
24. El-Ganainy, R. et al. Non-Hermitian physics and PT symmetry. *Nat. Phys.* **14**, 11–19 (2018).
25. Wang, X.-G., Guo, G.-H. & Berakdar, J. Steering magnonic dynamics and permeability at exceptional points in a parity–time symmetric waveguide. *Nat. Commun.* **11**, 5663 (2020).
26. Yang, Y. et al. Unconventional singularity in anti-parity–time symmetric cavity magnonics. *Phys. Rev. Lett.* **125**, 147202 (2020).
27. Zhang, D., Luo, X.-Q., Wang, Y.-P., Li, T.-F. & You, J. Q. Observation of the exceptional point in cavity magnon-polaritons. *Nat. Commun.* **8**, 1368 (2017).
28. Liu, H. et al. Observation of exceptional points in magnonic parity–time symmetry devices. *Sci. Adv.* **5**, 9144 (2019).
29. Liang, C., Tang, Y., Xu, A.-N. & Liu, Y.-C. Observation of exceptional points in thermal atomic ensembles. *Phys. Rev. Lett.* **130**, 263601 (2023).
30. Miri, M.-A. & Alù, A. Exceptional points in optics and photonics. *Science* **363**, 7709 (2019).
31. Chen, W., Özdemir, Ş. K., Zhao, G., Wiersig, J. & Yang, L. Exceptional points enhance sensing in an optical microcavity. *Nature* **548**, 192–196 (2017).
32. Hodaei, H. et al. Enhanced sensitivity at higher-order exceptional points. *Nature* **548**, 187–191 (2017).
33. Hokmabadi, M. P., Schumer, A., Christodoulides, D. N. & Khajavikhan, M. Non-Hermitian ring laser gyroscopes with enhanced Sagnac sensitivity. *Nature* **576**, 70–74 (2019).
34. Lai, Y.-H., Lu, Y.-K., Suh, M.-G., Yuan, Z. & Vahala, K. Observation of the exceptional-point-enhanced Sagnac effect. *Nature* **576**, 65–69 (2019).
35. Zhang, X., Hu, J. & Zhao, N. Stable atomic magnetometer in parity–time symmetry broken phase. *Phys. Rev. Lett.* **130**, 023201 (2023).
36. Wiersig, J. Enhancing the sensitivity of frequency and energy splitting detection by using exceptional points: Application to microcavity sensors for single-particle detection. *Phys. Rev. Lett.* **112**, 203901 (2014).
37. Peng, B. et al. Loss-induced suppression and revival of lasing. *Science* **346**, 328–332 (2014).
38. Wong, Z. J. et al. Lasing and anti-lasing in a single cavity. *Nat. Photon.* **10**, 796–801 (2016).
39. Huang, X., Lu, C., Liang, C., Tao, H. & Liu, Y.-C. Loss-induced nonreciprocity. *Light Sci. Appl.* **10**, 30 (2021).
40. Dong, S. et al. Loss-assisted metasurface at an exceptional point. *ACS Photon.* **7**, 3321–3327 (2020).
41. Feng, L. et al. Experimental demonstration of a unidirectional reflectionless parity–time metamaterial at optical frequencies. *Nat. Mater.* **12**, 108–113 (2013).
42. Li, Z. et al. Synergetic positivity of loss and noise in nonlinear non-hermitian resonators. *Sci. Adv.* **9**, 0562 (2023).
43. Park, J.-H. et al. Symmetry-breaking-induced plasmonic exceptional points and nanoscale sensing. *Nat. Phys.* **16**, 462–468 (2020).
44. Wang, H., Lai, Y.-H., Yuan, Z., Suh, M.-G. & Vahala, K. Petermann-factor sensitivity limit near an exceptional point in a Brillouin ring laser gyroscope. *Nat. Commun.* **11**, 1610 (2020).
45. Lau, H.-K. & Clerk, A. A. Fundamental limits and non-reciprocal approaches in non-Hermitian quantum sensing. *Nat. Commun.* **9**, 4320 (2018).
46. Kononchuk, R., Cai, J., Ellis, F., Thevamaran, R. & Kottos, T. Exceptional-point-based accelerometers with enhanced signal-to-noise ratio. *Nature* **607**, 697–702 (2022).
47. Ding, W., Wang, X. & Chen, S. Fundamental sensitivity limits for Non-Hermitian quantum sensors. *Phys. Rev. Lett.* **131**, 160801 (2023).
48. Zhang, M. et al. Quantum noise theory of exceptional point amplifying sensors. *Phys. Rev. Lett.* **123**, 180501 (2019).
49. Jacob, D., Vallet, M., Bretenaker, F., Le Floch, A. & Le Naour, R. Small Faraday rotation measurement with a Fabry–Pérot cavity. *Appl. Phys. Lett.* **66**, 3546–3548 (1995).
50. Zak, J., Moog, E. R., Liu, C. & Bader, S. D. Magneto-optics of multilayers with arbitrary magnetization directions. *Phys. Rev. B* **43**, 6423–6429 (1991).
51. Özdemir, Ş. K., Rotter, S., Nori, F. & Yang, L. Parity–time symmetry and exceptional points in photonics. *Nat. Mater.* **18**, 783–798 (2019).
52. Wiersig, J. Response strengths of open systems at exceptional points. *Phys. Rev. Res.* **4**, 023121 (2022).
53. Wiersig, J. Distance between exceptional points and diabolic points and its implication for the response strength of non-hermitian systems. *Phys. Rev. Res.* **4**, 033179 (2022).
54. Degen, C. L., Reinhard, F. & Cappellaro, P. Quantum sensing. *Rev. Mod. Phys.* **89**, 035002 (2017).
55. Hashemi, A., Busch, K., Christodoulides, D. N., Özdemir, Ş. K. & El-Ganainy, R. Linear response theory of open systems with exceptional points. *Nat. Commun.* **13**, 3281 (2022).
56. Takata, K. et al. Observing exceptional point degeneracy of radiation with electrically pumped photonic crystal coupled-nanocavity lasers. *Optica* **8**, 184–192 (2021).
57. Liang, J. et al. Polariton spin hall effect in a Rashba–Dresselhaus regime at room temperature. *Nat. Photon.* **18**, 357–362 (2024).

Methods

Derivation of the MO-induced coupling Hamiltonian

Here, we present a detailed derivation for the interaction Hamiltonian describing the MO-induced coupling between the HP and VP cavity modes. We first derive the relation between the MO constant and the Verdet constant. The magnetization **M** of a magnetic medium under an external magnetic field **B**, characterized by its general direction, can be defined in the (x, y, z)-coordinate system (Extended Data Fig. 1). We denote the amplitudes of the magnetization and the magnetic field with M and B, respectively. Using the polar angles φ and γ, the three orthogonal components of the magnetization are respectively

$$\begin{aligned} M_x &= M\sin\varphi\cos\gamma, \\ M_y &= M\sin\varphi\sin\gamma, \\ M_z &= M\cos\varphi. \end{aligned} \tag{4}$$

It is worth noting that the off-diagonal elements of the dielectric tensor are connected to the magnetization **M**. The MO effect originates from the off-diagonal terms. These terms have to obey the Onsager reciprocal relation under time reversal (reversing **B**)[8]. Thus, the dielectric tensor of the MO medium is expressed as[50]

$$\bar{\bar{\varepsilon}} = \varepsilon_0\varepsilon_s \begin{bmatrix} 1 & iQ\cos\varphi & -iQ\sin\varphi\sin\gamma \\ -iQ\cos\varphi & 1 & iQ\sin\varphi\cos\gamma \\ iQ\sin\varphi\sin\gamma & -iQ\sin\varphi\cos\gamma & 1 \end{bmatrix}, \tag{5}$$

where Q is the MO constant proportional to M and, thus, to magnetic field B, ε_0 is the vacuum permittivity and ε_s the relative dielectric constant of the medium in the absence of the external magnetic field, that is, the zero-field case. Hence, the components of the electric displacement vector **D**, given by $\mathbf{D} = \bar{\bar{\varepsilon}}\mathbf{E}$, where **E** represents the electric field of light. Generally, the MO constant is complex, $Q = Q_R + iQ_I$, where the real part Q_R and the imaginary part Q_I describe the magnetically induced circular birefringence and absorption, manifested by the polarization rotation and ellipticity of light in transmission and reflection in the conventional MO Faraday and Kerr effects. This electric constitutive relation can be rewritten in the general vector form as $\mathbf{D} = \varepsilon_0\varepsilon_s\mathbf{E} + i\varepsilon_0\varepsilon_s\frac{Q}{B}\mathbf{E}\times\mathbf{B}$ (ref. 8). This form allows one to study the more complicated MO effects and is of importance for deriving the coupling Hamiltonian.

We consider that light with wavelength λ propagates along the z axis in an MO medium. The HP (VP) component of the electric field of light, denoted as E_H (E_V), is along the x (y) axis. The corresponding unit polarization vectors are denoted as $\mathbf{e}_H$ and $\mathbf{e}_V$ such that $\mathbf{E}_H = E_H\mathbf{e}_H$ and $\mathbf{E}_V = E_V\mathbf{e}_V$. The corresponding propagation constant of light is $2\pi/\lambda$. When an external magnetic field is applied to the MO medium in z direction, we obtain $\varphi = 0$ and $\gamma = 0$. The dielectric tensor reduces to

$$\bar{\bar{\varepsilon}} = \varepsilon_0\varepsilon_s \begin{bmatrix} 1 & iQ & 0 \\ -iQ & 1 & 0 \\ 0 & 0 & 1 \end{bmatrix}. \tag{6}$$

Then, we have

$$\begin{aligned} \mathbf{D}_H &= (\varepsilon_0\varepsilon_s E_H + i\varepsilon_0\varepsilon_s Q E_V)\,\mathbf{e}_H, \\ \mathbf{D}_V &= (\varepsilon_0\varepsilon_s E_V - i\varepsilon_0\varepsilon_s Q E_H)\,\mathbf{e}_V, \end{aligned} \tag{7}$$

for the HP and VP components of the dielectric displacement vector in the medium, respectively. Importantly, the MO effect couples two cavity modes orthogonal in polarization. Using the relations $\mathbf{D}_+ = \frac{\mathbf{D}_H + i\mathbf{D}_V}{\sqrt{2}}$ and $\mathbf{D}_- = \frac{\mathbf{D}_H - i\mathbf{D}_V}{\sqrt{2}}$ to transfer the basis from the HP and VP to the RCP and the LCP, we can derive

$$\begin{aligned} \mathbf{D}_+ &= \varepsilon_0\varepsilon_s(1+Q)\tfrac{\mathbf{E}_H + i\mathbf{E}_V}{\sqrt{2}}, \\ \mathbf{D}_- &= \varepsilon_0\varepsilon_s(1-Q)\tfrac{\mathbf{E}_H - i\mathbf{E}_V}{\sqrt{2}}. \end{aligned} \tag{8}$$

Therefore, the MO medium exhibits the complex refractive indices $n_\pm^2 = \varepsilon_s(1 \pm Q)$ for the RCP and LCP fields. Here, $|Q| \ll 1$. We consider a complex value $\varepsilon_s = \varepsilon_s' + i\varepsilon_s''$ and $\varepsilon_s', \varepsilon_s'' > 0$, where its real part ε_s' and imaginary part ε_s'' reflect the refractive index and the absorption of the MO material. The refractive index of the host crystal is $n_s' = \sqrt{\varepsilon_s'}$. The zero-field absorption of the MO medium is characterized by $n_s'' \approx \varepsilon_s''/2\sqrt{\varepsilon_s'}$. For the transparent TGG crystal, we have $n_s''/n_s' \approx 1.63 \times 10^{-8}$ and $\varepsilon_s''/\varepsilon_s' = 2n_s''/n_s' \approx 3.3 \times 10^{-8}$ (Supplementary Section 2). Thus, we have $n_\pm \approx n_s'(1 \pm Q_R/2) + i(n_s'' \pm n_s'Q_I/2)$ (ref. 8). Typically, Q_R overwhelms Q_I by orders in amplitude. For example, $Q_R \approx 61Q_I$ even for the absorptive ferromagnetic material Fe (ref. 50). This ratio Q_R/Q_I is independent of the magnetic field B and at the level of 10^3 for the TGG crystal at $\lambda \approx 795$ nm (Supplementary Section 2).

Next, we connect the MO constant Q with the complex Verdet constant via the MO Faraday effect and derive the magnetically induced coupling Hamiltonian in the quantum formalism. We consider an L_{MO}-long MO medium with the Verdet constant C_V. The differential refractive indices causes a complex polarization rotation of $\theta = \theta_R + i\theta_I$ after a linearly polarized light beam passes through the medium. The real part of θ is the Faraday rotation. The imaginary part reflects the ellipticity of the transmitted light. The real and imaginary parts are respectively related to the MO constant via $\theta_R = \frac{2\pi}{\lambda}n_s'L_{MO}Q_R$ and $\theta_I = \frac{2\pi}{\lambda}n_s'L_{MO}Q_I$. According to the MO Faraday effect, we also have $\theta_R = C_V B L_{MO}$. Thus, we find the relation $Q_R = C_V B/k_s$, where k_s is the wave number of light in the MO medium and $k_s = 2\pi n_s'/\lambda$. When $Q_I \ll Q_R$, we can neglect the contribution of ε_s'' and Q_I. The constitutive relation reduces to $\mathbf{D} = \varepsilon_0\varepsilon_s\mathbf{E} + i\varepsilon_0\varepsilon_s\frac{C_V}{k_s}\mathbf{E}\times\mathbf{B}$.

For an L_c-long FP cavity embedded with an L_{MO}-long MO medium, the Hamiltonian describing the system energy is given by

$$H_s = \int_V \mathbf{D}^*(r)\cdot\mathbf{E}(r)\mathrm{d}V. \tag{9}$$

Here, we use the complex magnitude for the displacement and the electric field, for simplicity. We neglect the contribution from the energy of the magnetic field of light because it shifts the system energy only by a constant value in this MO model. In the case of $B = 0$, we can decompose the free Hamiltonian into two contributions from the bare FP cavity and the MO medium as

$$H_0 = \int_{V_c} \mathbf{D}^*(r)\cdot\mathbf{E}(r)\mathrm{d}v + \int_{V_{MO}} \frac{\varepsilon_s - 1}{\varepsilon_s}\mathbf{D}^*(r)\cdot\mathbf{E}(r)\mathrm{d}v, \tag{10}$$

where V_c and V_{MO} are the volumes of light field in the bare FP cavity and the MO medium, respectively. Equation (10) is the free Hamiltonian in the HP and VP basis. The HP and VP eigenmodes are decoupled in the absence of the magnetic field B. They are degenerate in frequency such that $\nu_H = \nu_V = \nu_0$. We use notations a_H and a_V for denoting the annihilation operators of the quantized HP and VP eigenmodes. We assume that the mode effective volume is V_m and the amplitude of the quantum vacuum field is E_0 such that the system energy is $h\nu_0 = \varepsilon_0 V_m E_0^2/2$. The ratio of the optical volume of light in the MO medium and the cavity volume is given by $\eta = V_{MO}/V_c = L_{MO}/L_c$. At $B = 0$, this free Hamiltonian in operators takes the form

$$H_0 = h\nu_0\left(a_H^\dagger a_H + a_V^\dagger a_V\right). \tag{11}$$

In the presence of the magnetic field B, the HP and VP modes are coupled via the MO effect. The interaction Hamiltonian is given by

$$H_I = i\varepsilon_0(\varepsilon_s - 1)Q\int_{V_{MO}} \left(E_V^* E_H - E_H^* E_V\right)\mathrm{d}V. \tag{12}$$

In the presentation of the quantized HP and VP cavity modes, the Hamiltonian in quantum optics becomes

$$\begin{aligned} H_I &= i\varepsilon_0(\varepsilon_s - 1)QV_{MO}E_0^2\left(a_V^\dagger a_H - a_H^\dagger a_V\right) \\ &= ih\nu_0(\varepsilon_s - 1)Q\eta\left(a_V^\dagger a_H - a_H^\dagger a_V\right). \end{aligned} \tag{13}$$

We rewrite the interaction Hamiltonian in the standard form as

$$H_{\mathrm{I}} = ihgB\left(a_{\mathrm{V}}^{\dagger}a_{\mathrm{H}} - a_{\mathrm{H}}^{\dagger}a_{\mathrm{V}}\right), \tag{14}$$

with the complex coefficient $g = g_{\mathrm{R}} + ig_{\mathrm{I}}$ and $g_{\mathrm{R}} = (\varepsilon_s' - 1)\eta C_{\mathrm{V}} v_0/k_s$ for the real part of the MO-induced interaction. Interestingly, the MO effect can also induce an anti-Hermtian interaction with strength $g_{\mathrm{I}}B = \varepsilon_s''\eta Q_{\mathrm{R}} + (\varepsilon_s' - 1)\eta Q_{\mathrm{I}} \approx (\varepsilon_s' - 1)\eta Q_{\mathrm{I}}$ due to $\varepsilon_s'' \ll \varepsilon_s'$, apart from a Hermitian interaction. Essentially different from the chiral optical cavity embedded with a natural optical active medium, the magnetic field simultaneously breaks the TRS. As a result, the MO effect accumulates a non-zero interaction between the HP and VP modes. The general full Hamiltonian for the system is

$$H = h\left(v_{\mathrm{H}}a_{\mathrm{H}}^{\dagger}a_{\mathrm{H}} + v_{\mathrm{V}}a_{\mathrm{V}}^{\dagger}a_{\mathrm{V}}\right) + ihg_{\mathrm{R}}B\left(a_{\mathrm{V}}^{\dagger}a_{\mathrm{H}} - a_{\mathrm{H}}^{\dagger}a_{\mathrm{V}}\right) - hg_{\mathrm{I}}B\left(a_{\mathrm{V}}^{\dagger}a_{\mathrm{H}} - a_{\mathrm{H}}^{\dagger}a_{\mathrm{V}}\right). \tag{15}$$

The second part describes the MO-induced Hermitian Hamiltonian, which means that there is a non-reciprocal coupling between the two cavity modes because the two off-diagonal elements are unequal. The third part represents the anti-Hermitian interaction dominantly originating from the MO-induced absorption[8,58]. The latter is normally negligibly small with respect to the former. Phenomenally taking into account the cavity decay with rates κ_{H} and κ_{V} for the HP and VP modes, respectively, and neglecting the anti-Hermitian interaction, we obtain

$$H = h\begin{bmatrix} v_{\mathrm{H}} - i\kappa_{\mathrm{H}} & igB \\ -igB & v_{\mathrm{V}} - i\kappa_{\mathrm{V}} \end{bmatrix}. \tag{16}$$

For the TGG crystal, g is real (Supplementary Section 2), to a good approximation. This quantum Hamiltonian provides a formalism beyond the classical picture of polarization rotation and ellipticity of light and reveals richer physics underlying the MO effect. In particular, it provides a convenient model and a transparent picture for understanding the mode coupling in an optical cavity and the related non-Hermitian physics.

It is interesting to address the symmetry of the Hamiltonian with $v_{\mathrm{H}} = v_{\mathrm{V}}$ and non-zero real gB. We define the rotation operator as

$$R_\theta = \begin{bmatrix} \mathrm{e}^{i\theta} & 0 \\ 0 & \mathrm{e}^{-i\theta} \end{bmatrix}, \tag{17}$$

with $R_\theta^{-1} = R_{-\theta}$, and the standard parity operator as

$$\mathcal{P} = \begin{bmatrix} 0 & 1 \\ 1 & 0 \end{bmatrix}. \tag{18}$$

We can define a rotation–parity operator $R_\theta\mathcal{P}$ as

$$\mathcal{P}_\theta = \begin{bmatrix} 0 & \mathrm{e}^{i\theta} \\ \mathrm{e}^{-i\theta} & 0 \end{bmatrix}. \tag{19}$$

We dub it the generalized parity operator. The time reversal $\mathcal{T}$ changes i to $-i$. If κ_{H} and κ_{V} are positive, we can apply a gauge transformation to the eigenmodes. For a Hermitian system with $\kappa_{\mathrm{H}} = \kappa_{\mathrm{V}}$, the Hermitian H obeys the rotation–parity symmetry under operation $\mathcal{P}_{\pi/2}H\mathcal{P}_{\pi/2}^{-1} = H$ but $\mathcal{P}H\mathcal{P}^{-1} \neq H$. For simplicity, we refer to the parity symmetry in the main text as the generalized parity symmetry. Under the gauge transformation, the non-Hermitian system with $\kappa_{\mathrm{H}} \neq \kappa_{\mathrm{V}}$ obeys $(\mathcal{PT})H(\mathcal{PT})^{-1} = H$, implying the passive $\mathcal{PT}$ symmetry without involving the gain.

Measurement of Verdet constant of the TGG crystal

Due to the difference in refractive index between RCP and LCP in a TGG crystal, a linearly polarized laser beam experiences rotation after passing through the TGG crystal. The rotation angle $\alpha = C_{\mathrm{V}}BL_{\mathrm{mo}}$, where C_{V} is the Verdet constant and L_{mo} represents the length of the TGG crystal. In an optical cavity, we can derive that $\alpha = \frac{\pi}{2}\frac{\Delta\nu}{\mathrm{FSR}}$. During measurement, we use a small magnetic loop to generate the magnetic field, instead of the current coil. We fix the magnitude of magnetic field at 194 mT and scan the laser wavelength. The Verdet constant of the TGG crystal has been measured from 765 nm to 804 nm, as shown in Extended Data Fig. 2. We fitted the experimental data with the formula given by[59]

$$C_{\mathrm{V}} = \frac{C_{\mathrm{f}}}{\lambda^2 - \lambda_{\mathrm{f}}^2}, \tag{20}$$

where the fitting parameters are $C_{\mathrm{f}} = 4.45149 \times 10^7$ rad nm^2 T^{-1} m^{-1} and $\lambda_{\mathrm{f}} = 257.5$ nm. The Verdet constant (C_{V}) is measured to be 78.82 rad T^{-1} m^{-1} ($\lambda = 795$ nm).

Data availability

The data that support the plots within this paper are available via figshare at https://doi.org/10.6084/m9.figshare.25998517(ref. 60). All other data used in this study are available from the corresponding authors upon reasonable request.

References

58. Opechowski, W. Magneto-optical effects and paramagnetic resonance. *Rev. Mod. Phys.* **25**, 264–268 (1953).
59. Víllora, E. G. et al. Faraday rotator properties of $Tb_3(Sc_{1.95}Lu_{0.05})Al_3O_{12}$, a highly transparent terbium-garnet for visible-infrared optical isolators. *Appl. Phys. Lett.* **99**, 011111 (2011).
60. Ruan, Y.-P. et al. Observation of loss-enhanced magneto-optical effect. *figshare* https://doi.org/10.6084/m9.figshare.25998517 (2024).

Acknowledgements

This work was supported by the National Natural Science Foundation of China (grant nos. 92365107, 12334012, 12234012, 12305020, 11935006 and 12421005), the National Key R&D Program of China (grant nos. 2019YFA0308700, 2019YFA0308704, 2022YFA1405000, 2021YFA1400900, 2021YFA0718300 and 2024YFE0102400), the Innovation Program for Quantum Science and Technology (grant nos. 2021ZD0301400 and 2021ZD0301500), the Program for Innovative Talents and Teams in Jiangsu (grant no. JSSCTD202138), the Natural Science Foundation of Jiangsu Province, Major Project (grant no. BK20212004), the Hunan Major Sci-Tech Program (grant no. 2023ZJ1010), the China Postdoctoral Science Foundation (grant no. 2023M731613) and Jiangsu Funding Program for Excellent Postdoctoral Talent (grant no. 2023ZB708). C.-W.Q. acknowledges the support from National Research Foundation (grant no. NRF2021-QEP2-03-P09 with WBS number A-8000708-00-00 and grant no. NRF-CRP26-2021-0004).

Author contributions

K.X. conceived the original idea and the research, and supervised the project. W.L., H.J., Y.-Q.L. and C.-W.Q. contributed to the idea and co-supervised the project. Y.-P.R. conducted the experiment and performed the data analysis and processing. J.-S.T., Z.L., Y.-P.R., W.L., H.J., C.-W.Q. and K.X. contributed to the theoretical model and interpretation of experimental results. K.X. presented the electric constitutive relation and solely derived the interaction Hamiltonian. H.W., W.Z. and H.Z. contributed to the experimental implementation and details. S.-J.G. and W.H. fabricated the LC cell. J.C., Z.L., Y.-Q.L., W.L., H.J., C.-W.Q. and K.X. developed the underlying physics. Y.-P.R., Z.L., J.C., W.L., H.J., J.-S.T., C.-W.Q. and K.X. contributed to manuscript writing. All authors contributed to discussion of experimental data and results.

Competing interests
The authors declare no competing interests.

Additional information
Extended data is available for this paper at https://doi.org/10.1038/s41566-024-01592-y.

Supplementary information The online version contains supplementary material available at https://doi.org/10.1038/s41566-024-01592-y.

Correspondence and requests for materials should be addressed to Cheng-Wei Qiu, Wuming Liu, Hui Jing, Yan-Qing Lu or Keyu Xia.

Peer review information *Nature Photonics* thanks Vladimir Belotelov, Jan Wiersig and the other, anonymous, reviewer(s) for their contribution to the peer review of this work.

https://doi.org/10.1038/s41566-024-01592-y

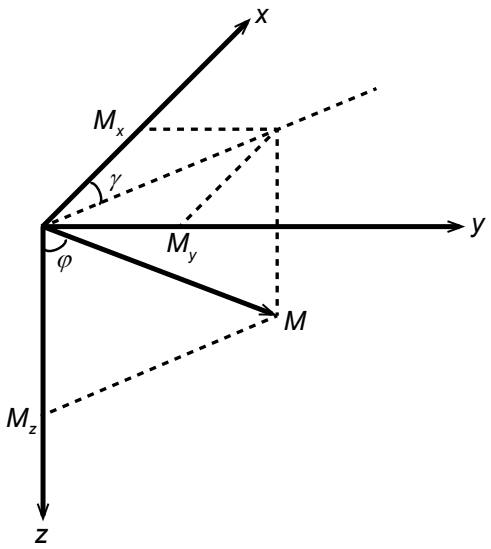

Extended Data Fig. 1 | Spherical coordinate system for the magnetization *M* in the (*x*, *y*, *z*)-coordinate. The angle φ represents the orientation of *M* with respect to the *z* axis, and γ is the angle between *M* projected on the *x*-*y* plane and the *x* axis[50].

https://doi.org/10.1038/s41566-024-01592-y

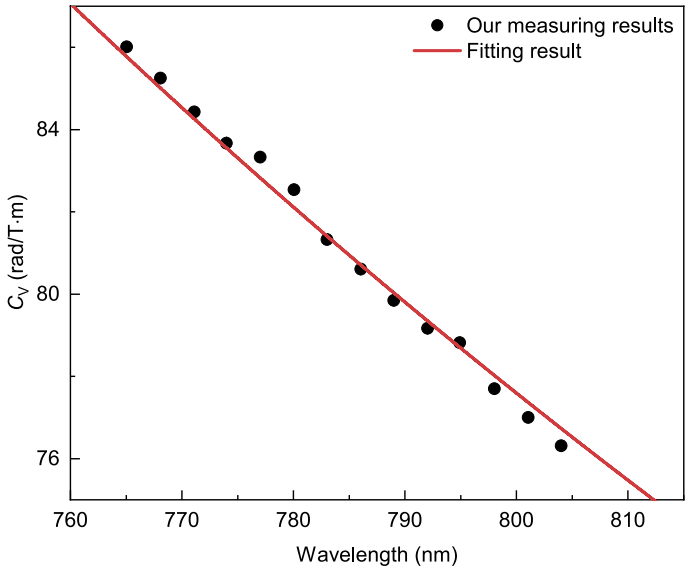

Extended Data Fig. 2 | Verdet constant of the TGG crystal. Black dots represent the experimental results and red curve represents the fitting from ref. 59.